

Comparison of methods used to derive the Galactic star formation history from white dwarf samples

Emily K. Roberts,¹^{*} Pier-Emmanuel Tremblay,¹ Mairi W. O’Brien,¹ Antoine Bédard,¹ Tim Cunningham,²[†]
 Conor M. Byrne,¹ and Elena Cukanovaite¹

¹ Department of Physics, University of Warwick, Coventry CV4 7AL, UK

² Center for Astrophysics, Harvard & Smithsonian, 60 Garden St., Cambridge, MA 02138, USA

Accepted XXX. Received YYY; in original form ZZZ

ABSTRACT

We compare three methods of deriving the local Galactic star formation history, using as a benchmark the *Gaia*-defined 40 pc white dwarf sample, currently the largest volume complete sample of stellar remnants with medium-resolution spectroscopy. We create a population synthesis model to 1) reproduce the observed white dwarf luminosity function, 2) reproduce the observed absolute *Gaia* *G* magnitude distribution, and 3) directly calculate the ages of all individual white dwarfs in the 40 pc volume. We then compare the star formation histories determined from each method. Previous studies using these methods were based on different white dwarf samples and as such were difficult to compare. Uncertainties in each method such as the initial mass function, initial-final mass relation, main sequence lifetimes, stellar metallicity, white dwarf cooling ages and binary evolution are accounted for to estimate the precision and accuracy of each method. We conclude that no method is quantitatively better at determining the star formation history and all three produce star formation histories that agree within uncertainties of current external astrophysical relations.

Key words: white dwarfs – stars: luminosity function – stars: evolution – Galaxy: solar neighbourhood

1 INTRODUCTION

The topic of galaxy formation and evolution is one that underpins many different areas of astronomy, from the history of individual galaxies to the specifics of the cosmological model used (Stewart et al. 2008). Studying the history of the Milky Way is beneficial to understanding similar field galaxies. From simulations using Λ CDM frameworks, 95 per cent of galaxies like the Milky Way have experienced a small merger event in the last 10 Gyr (Stewart et al. 2008), making it likely that the Milky Way will have experienced one too. There has also been evidence of star formation quenching in the Milky Way’s history (Haywood et al. 2018) which follows after merger events as shown by simulations using Λ CDM frameworks such as Di Matteo et al. (2008) or by the presence of a galactic bar (Haywood et al. 2016; Khoperskov et al. 2018). Merger events can therefore trigger star formation bursts or lulls that could be detectable in the star formation history (Helmi et al. 2018; Antoja et al. 2018).

The star formation rate tells us how many stars formed at a given time in a population’s history and is one way to investigate the evolution of a galaxy. The star formation rate is a time-varying function that spans the whole lifetime of the population under study and forms the star formation history of the subject; as such, these two terms are often used interchangeably. Many different methods have been developed to probe the star formation history on galaxy-wide scales, such as

resolving features of colour-magnitude diagrams (Weisz et al. 2008), measurements of IR dust emission (Rieke et al. 2009), and near-UV emission measurements to trace recent (in the last 10–200 Myr) star formation (Salim et al. 2007). Methods focussed specifically on the Milky Way’s star formation history can use more detailed information on individual stars. Mor et al. (2019), for example, use simulated colours, magnitudes, and parallaxes compared to *Gaia* Data Release 2 to infer the star formation rate of the Galactic disc. Nucleocosmochronology may also prove a valuable tool in age determinations of individual stars and therefore star formation histories (Ludwig et al. 2010). There are other methods that use kinematics, isochrones, or asteroseismology (see Soderblom 2010 and references therein for a review), providing a plethora of approaches to the field.

Methods that only use white dwarf stars have also been employed, such as observing and modelling the luminosity function (Winget et al. 1987; Rowell 2013), calculating the ages of individual white dwarfs (Tremblay et al. 2014; Kilic et al. 2019), and modelling the absolute magnitude distribution (Cukanovaite et al. 2023). White dwarf stars are the electron degenerate remnants of main sequence stars with masses of less than 8 – 10 M_{\odot} depending on metallicity (Iben et al. 1997). Because white dwarfs have no nuclear fuel of their own, they cool predictably with a high dependence on age (Mestel 1952) making them potential chronometers. However, their practicality as chronometers has until recently been hindered by the fact that, by their nature, white dwarfs are faint and harder to observe.

With the advent of *Gaia*, our ability to use white dwarfs in this manner has been revolutionised by the quantity and quality of observational data (Gaia Collaboration et al. 2016a,b, 2018, 2021). The

^{*} E-mail: Emily.Roberts.1@warwick.ac.uk

[†] NASA Hubble Fellow

cataloguing of *Gaia* white dwarfs from Data Release 2 (Jiménez-Esteban et al. 2018; Gentile Fusillo et al. 2019) and early Data Release 3 (Gentile Fusillo et al. 2021) provides far larger samples on which to apply previously established methods as well as opportunities for new methods for estimating stellar formation histories. The full potential of *Gaia* data has yet to be explored.

Despite the advances made possible by *Gaia*, in any full model of a stellar population and its history there remain many systematic uncertainties, both from *Gaia* data itself and other underlying assumptions made in modelling. In particular, even with the same method of determining the star formation history of a population, one may use different astrophysical relations, for example different initial-final mass relations, to map the mass of a main sequence star to its final mass as a white dwarf, or white dwarf evolutionary models. While most previous attempts to derive the star formation history of the solar neighbourhood have included systematic uncertainties in their analyses, significantly different histories were inferred from various white dwarf (Schröder et al. 2004; Rowell 2013; Tremblay et al. 2014; Fantin et al. 2019; Isern 2019; Cukanovaite et al. 2023) and main-sequence studies (Cignoni et al. 2006; Mor et al. 2019; Alzate et al. 2021; Dal Tio et al. 2021; Gallart et al. 2024). It is unclear if these differences arise from different analysis methods and their systematics or different data sets.

In this work, we therefore use the same white dwarf sample to compare three methods of deriving the star formation history of a population: the white dwarf luminosity function, the absolute magnitude distribution and direct age calculations. We use the same external systematic uncertainties from astrophysical relations for each method to investigate whether there is a quantitatively best method, and a consistently best fitting star formation history for the local Galactic population. We present a comparison of the three methods and the best fitting star formation history as chosen by each of the three methods. We also look at the systematic errors that affect modelling white dwarf populations and explore which areas may require future work to help constrain Galactic models further.

One way to lessen data biases is to use a volume complete sample of stars. In this work, we focus on the population within 40 pc of the Sun, and the local star formation history inferred from white dwarfs (Cukanovaite et al. 2023). This volume-complete sample of 1073 white dwarfs from *Gaia* Data Release 3 that have been spectroscopically confirmed was outlined in O’Brien et al. (2024).

In Section 2 we outline the *Gaia* 40 pc sample of white dwarfs. Section 3 describes the three stellar formation history methods we have compared using the 40 pc sample. Section 4 looks at the systematic uncertainties that govern each method, which are discussed in Section 5. Finally, we discuss the conclusions of this work in Section 6.

2 THE 40 PC SAMPLE OF WHITE DWARFS

Our sample is comprised of all white dwarf candidates from *Gaia* Data Release 3 in the Gentile Fusillo et al. (2021) catalogue, located within 40 pc of the Sun, and spectroscopically confirmed (O’Brien et al. 2024). This gives a total of 1073 white dwarfs, of which 658 are listed as DA white dwarfs for their primary spectral type (showing hydrogen spectral features), 17 are listed as DB white dwarfs (showing neutral helium spectral features), 285 are featureless DC white dwarfs, while the remaining 113 are a mixture of DQs with detectable carbon features, DZs with detectable metal lines, and DXs which are dependent on individual analysis (see O’Brien et al. 2024 and refer-

ences therein for individual spectral types). For all the values listed here, the spectral type listed, e.g. DA, includes all sub-types such as DAZ, DAQ, etc. Excluding DC white dwarfs below 5000 K with unconstrained compositions, 77.5 per cent of the sample have hydrogen dominated atmospheres and 22.5 per cent have helium dominated atmospheres. All white dwarfs have published atmospheric and stellar parameters appropriate for their atmospheric compositions (Gentile Fusillo et al. 2021; Caron et al. 2023; O’Brien et al. 2024; Vincent et al. 2024).

If a population of white dwarfs evolves according to single star evolution, we expect a constant median mass (Tremblay et al. 2016) of $\approx 0.6 M_{\odot}$ (e.g. McCleery et al. 2020) across all temperatures. However, when fitting the white dwarf photometry and *Gaia* parallax, the median mass drops significantly below ≈ 6000 K, most likely due to inaccuracies in opacities such as the red wing of Ly α (Caron et al. 2023) rather than binary evolution causing genuine lower masses. This low mass issue was corrected for in O’Brien et al. (2024) using a fifth-order polynomial to bring *Gaia* masses in line with the expected constant median mass. To predict the same absolute *G* magnitude, the corresponding effective temperatures were also corrected using the white dwarf mass-radius relation (Bédard et al. 2020).

The other issue regarding mass determinations in the 40 pc sample is the appearance of seemingly low mass white dwarfs (below $\approx 0.54 M_{\odot}$) which have predicted total lifetimes longer than that of the Universe. These white dwarfs are understood to be either statistical outliers, unresolved double degenerate systems erroneously assumed to be a single white dwarf in the *Gaia* fitting procedure, or more rarely within a volume, true low mass white dwarfs that went through binary evolution (Cunningham et al. 2024; O’Brien et al. 2024). By having two objects within *Gaia*’s spatial resolution limit, if a single white dwarf with the luminosity of the two objects is assumed, it makes the radius much larger and, consequently, the mass much lower than is physically possible for a single white dwarf within the age of the Universe. Because the vast majority of double degenerate candidates within 40 pc are unconfirmed and the minimum mass of a single white dwarf is uncertain (Kalirai 2012; Cummings et al. 2018; El-Badry et al. 2018; Marigo et al. 2020; Hollands et al. 2024; Cunningham et al. 2024), a sharp cut off at $0.54 M_{\odot}$ to exclude all white dwarfs below this mass was deemed the best compromise for the purpose of method comparison analysis.

In Fig. 1, we show the mass distribution for the 40 pc sample with and without the low-mass correction accounting for opacity modelling issues, as well with the vertical double degenerate cut off line at $0.54 M_{\odot}$. The rest of this work was conducted on the sample of 960 objects with corrected masses above $0.54 M_{\odot}$.

The 40 pc sample has, as mentioned, both DA and non-DA spectral types within it. There are some advantages to using the DA-only sample, for example the *Gaia* derived masses are more reliable for DA spectral types (Cunningham et al. 2024) since non-DA white dwarfs have trace elements (H, C) that can impact mass determinations (Bergeron et al. 2019; Blouin et al. 2023; Camisassa et al. 2023; Kilic et al. 2025). A DA-only sample also reduces the effect of the low mass corrections as DA white dwarfs do not exist below ≈ 5000 K since H α is not detectable, although this introduces a strong cooling age bias. Similarly, a cut-off on lower-than-average mass white dwarfs can reduce uncertainties on stellar parameters by removing objects with long main-sequence lifetimes (Isern 2019; Heintz et al. 2022), again introducing biases on stellar ages, in part because more massive white dwarfs are more likely to be stellar merger remnants (Temink et al. 2020). As our work is attempting to replicate the entire 40 pc sample and investigate the underlying star formation history, as well

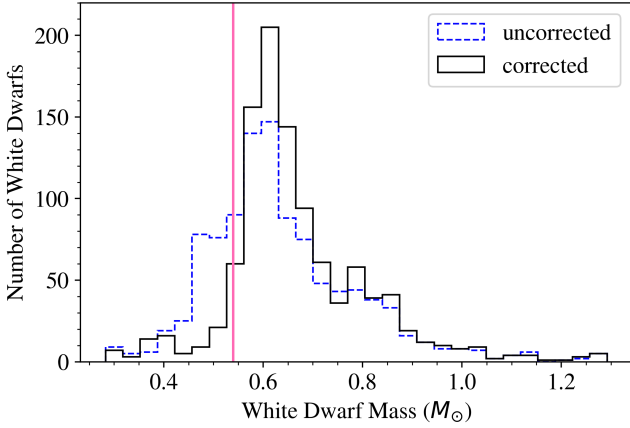


Figure 1. Photometric white dwarf mass distribution of the *Gaia* 40 pc sample (blue dashed line) compared with the mass distribution after the low mass corrections of O’Brien et al. (2024) for cool white dwarfs ($T_{\text{eff}} < 6000$ K) is applied (black solid line). The vertical (pink) line represents the lower mass cut off, below which the objects are considered to be double degenerate and other binary white dwarfs and are excluded from this work.

as evaluate methods for doing so, we use the full 40 pc white dwarf sample.

3 METHODS UNDER COMPARISON

In order to compare different methods of using white dwarfs to determine the star formation history of a population, we identified three independent methods that could be tested on the 40 pc sample.

The first two methods use forward modelling to simulate a synthetic population of white dwarfs with properties that can be quantitatively compared to the observed 40 pc sample. We look at 1.) the luminosity function (the absolute bolometric magnitude distribution) and 2.) the absolute *Gaia* G magnitude distribution of the sample. Despite using the same simulation to generate the synthetic white dwarf population, the calculations of luminosity/bolometric magnitude and absolute G magnitude rely on different subsets of *Gaia* data: luminosity and bolometric magnitude depend on the derived effective temperature and mass whereas absolute G magnitude is a function of apparent G magnitude and parallax.

The third employed method infers the age of each white dwarf in the sample from its effective temperature and mass, directly reconstructing the star formation history. By working in reverse, this method is also independent.

The three methods do share many ingredients and systematic uncertainties, such as the initial mass function and initial-final mass relation. The default values of these shared ingredients are listed in Table 1, while systematic uncertainties on these ingredients are discussed in Section 4.

3.1 Luminosity function

In our simulations, 30 000 stars are generated according to the initial mass function (Salpeter 1955). Their main sequence and post-main sequence lifetimes up to and including the asymptotic giant branch phase are then assigned according to the latest single-star

Binary Population and Spectral Synthesis (BPASS, Eldridge et al. 2017; Stanway & Eldridge 2018) detailed stellar evolution models presented in Byrne et al. (2024), assuming solar metallicity for all stars. To assign each star a formation time, a star formation history has to be assumed. Formation times are sampled from an assumed star formation history from a lookback time of $t = 0$ (the present day) to $t = t_{\text{pop age}}$ (the population age of the simulation, 10.6 Gyr by default, see Cukanovaite et al. 2023) to give each star an age.

White dwarfs are assigned masses based on a newly derived, self-consistent initial-final mass relation where our methodology closely follows the one outlined in Cunningham et al. (2024). The initial-final mass relation is constructed using the derived *Gaia* masses for the entire 40 pc white dwarf sample. However, since Cunningham et al. (2024) used main-sequence lifetimes from Hurley et al. (2000), here we re-calculated the initial-final mass relation using the same code but swapping for the BPASS stellar lifetimes. This ensures self-consistency, e.g. for our maximum population age (10.6 Gyr) and minimum white dwarf mass for single star evolution ($0.54 M_{\odot}$), the BPASS lifetime of the corresponding main-sequence star cannot be larger than 10.6 Gyr. We note that this is a significant difference compared to the stellar population synthesis work of Cukanovaite et al. (2023) for the 40 pc sample, who used the initial-final mass relation of El-Badry et al. (2018).

It is known that older groups of stars have a higher velocity dispersion in all three Galactic coordinates (Rowell & Kilic 2019) and so are more likely than younger stars to have left the local 40 pc volume, which is within the Galactic plane where open clusters dominate stellar formation. McCleery et al. (2020) only found four halo white dwarfs in the 40 pc sample, for example. We assume that equal numbers of stars enter and leave the volume in the simulated x and y directions parallel to the Galactic plane. Only in the z direction, perpendicular to the Galactic disc, stars will be leaving and entering the volume at different rates. This allows us to use a one dimensional correction. Using the calculations detailed in Cukanovaite et al. (2023) to relate the total age of a star, t_{total} in Gyr, to its scale height, h in pc, we calculate the probability p of a star having left the volume as:

$$h = 10.71(t_{\text{total}}) + 65, \quad (1)$$

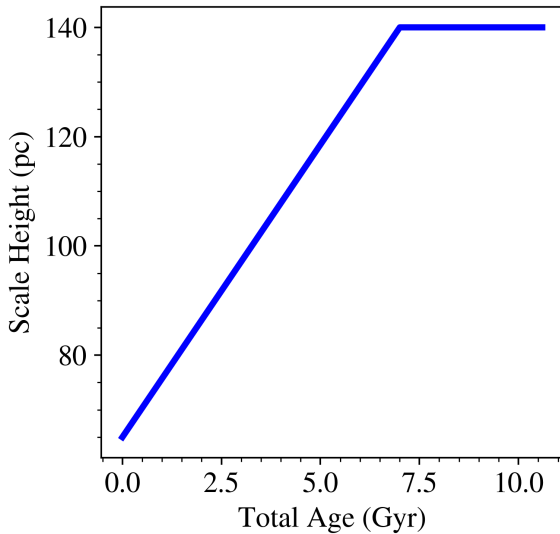
$$p(\text{left}) = 1 - 65/h. \quad (2)$$

The derived scale height as a function of age is shown in Fig. 2. The flattening of this function at 140 pc is due to a lack of evidence for kinematics evolution of stars older than around 7 Gyr (Seabroke & Gilmore 2007). Only stars that have not left the 40 pc volume over the course of their lifetime are kept in the simulation.

White dwarfs that are remnants of binary mergers are predicted to make up 10 – 30 per cent of single observable white dwarfs (Temminck et al. 2020) and only more recent simulations of white dwarf populations have included such an effect (Toonen et al. 2017; Kilic et al. 2020; Cukanovaite et al. 2023). This variable is included in our work through the default models of binary populations of Temminck et al. (2020), primarily the merger fraction as a function of white dwarf mass, and the differences in inferred white dwarf formation time as a function of white dwarf mass. For each simulated white dwarf, we calculate the probability of it having formed via binary merger of any type, and then, if it did form this way, we sample the delay this would apply to its cooling from a Gaussian distribution with the mean and standard deviation taken from the quartiles shown in Fig. 6 of Temminck et al. (2020). The probability of a star forming via binary merger is dependent on mass, as shown in the top plot of Fig. 3, and the cooling delay applied to each star in the simulation can be seen in the bottom plot of Fig. 3. The blue points in the bottom

Table 1. The list of default astrophysical relations used to construct the synthetic population of white dwarfs used in the Luminosity Function and Absolute G Magnitude Distribution methods, and to calculate the ages of individual white dwarfs in the Direct Age method.

Ingredient	Key information	Source
Population age	10.6 Gyr	Cukanovaite et al. (2023)
Initial mass range	0.95–6.84 M_{\odot}	Cunningham et al. (2024)
Initial mass function	$\rho(M) \propto M^{-2.35}$	Salpeter (1955)
Initial metallicity	$Z = Z_{\odot} = 0.0134$ for all stars generated	Asplund et al. (2009)
Main sequence + giant phases lifetimes	Function of mass and metallicity	Byrne et al. (2024)
Initial-final mass relation	Four piece segmented linear fit	This work (see Cunningham et al. 2024)
He-atmosphere WD fraction	≈ 0.25 (temperature-dependent)	O’Brien et al. (2024)
Merger delays	Probability of forming via merger is a function of mass	Temminck et al. (2020)
Age vs. kinematic relation	$h(\text{scale height in pc}) = 10.71(t_{\text{total}}) + 65$ $p(\text{probability left volume}) = 1 - 65/h$	Cukanovaite et al. (2023)
Cooling models	Theoretical cooling sequences of C/O core white dwarfs	Bédard et al. (2020)
Crystallisation cooling delay	Extra 0.5 Gyr to cooling at crystallised mass fraction of 0.5	Blouin et al. (2020); Kilic et al. (2020)

**Figure 2.** Scale height as a function of the total age of a star. This linear relationship is derived in Cukanovaite et al. (2023) and flattens off at 140 pc due to a lack of evidence for kinematic evolution of stars older than around 7 Gyr (Seabroke & Gilmore 2007).

plot show that this cooling delay is not always a delay: the majority of the time the difference is positive and it decreases the white dwarf cooling time for the same assumed formation history; less commonly it is negative and increases the cooling time. Accounting for binary evolution produces on average hotter and brighter white dwarfs for the same formation history than when compared to a population with binary evolution unaccounted for.

To determine which stars in the simulation have become white dwarfs by the present day, the white dwarf cooling time for each star is calculated as:

$$t_{\text{WD}} = t_{\text{total}} - t_{\text{MS+GP}} - t_{\Delta} \quad (3)$$

where t_{WD} is the cooling time of the white dwarf, t_{total} is the formation time of the star and its total age, $t_{\text{MS+GP}}$ is the main sequence

and giant phases lifetime of the star, and t_{Δ} is the change in cooling time due to a merger history. Stars with a negative white dwarf cooling time have not had enough time since their formation to evolve into white dwarfs by the present day, and are discarded from the simulation.

It is worth noting that we also deal with unresolved binarity in two additional ways: as previously mentioned, we employ a mass cut off of $0.54 M_{\odot}$ that removes the majority of unresolved double degenerate systems from the observed 40 pc sample; also, unresolved white dwarf and main sequence pairs are selected against in the observational sample as it is constructed from the *Gaia* white dwarf catalogue of Gentile Fusillo et al. (2021) which does not select white dwarfs with a large red excess from a main-sequence companion (O’Brien et al. 2024).

The cooling models of Bédard et al. (2020) depend on the envelope composition of the white dwarf, either hydrogen-rich or hydrogen-deficient. The cooling models assume a carbon/oxygen core (50/50 proportions in mass), a helium mantle ($M_{\text{He}}/M_{\text{WD}} = 10^{-2}$), and either a thick or thin hydrogen outer layer ($M_{\text{H}}/M_{\text{WD}} = 10^{-4}$ or 10^{-10} , respectively). White dwarfs with standard thick hydrogen layers retain a hydrogen-rich atmosphere for their entire evolution, while hydrogen-deficient white dwarfs exhibit a variable atmospheric composition (and thus spectral type) with cooling age (Bédard 2024). In this work, we follow the usual convention of modelling hydrogen-atmosphere objects with thick-layer cooling models, and helium-atmosphere objects with thin-layer cooling models. While this does ignore some elements of spectral evolution, given that some thin-layer white dwarfs have hydrogen-rich atmospheres, the simplifying assumption used here has a negligible impact on the 40 pc sample simulations as fewer than 1% of the sample are thin-layer white dwarfs with hydrogen-rich atmospheres.

The evolution of the fraction of helium-atmosphere white dwarfs with temperature is determined by Fig. 6 of O’Brien et al. (2024). The increasing number of helium-atmospheres with decreasing T_{eff} is thought to originate from the convective mixing of a thin superficial hydrogen layer in the larger underlying helium layer (Rolland et al. 2018; Cunningham et al. 2020; Bédard et al. 2022). Regarding spectral types and predicted colours, we implement this atmosphere composition versus T_{eff} dependence in a probabilistic way,

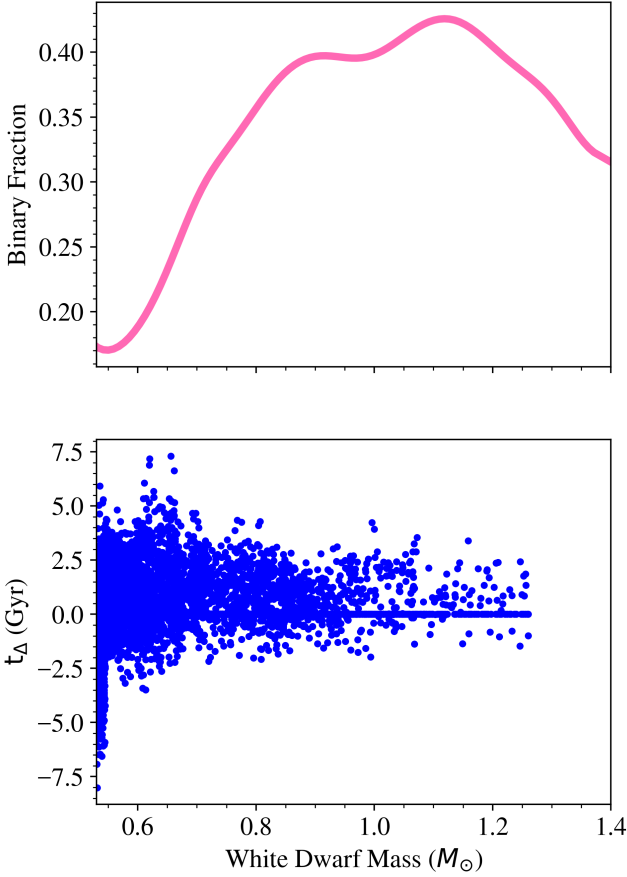


Figure 3. *Top:* The fraction of white dwarfs that formed with a merger in their past as a function of white dwarf mass. This is the default model of Temmink et al. (2020). *Bottom:* The time differences in Gyr between the evolutionary history of a white dwarf assuming single star evolution and binary evolution for the stars in the default synthetic population of this work assuming constant formation history. If a star was not formed via binary evolution, the time difference is zero. If it did form via binary evolution and the time difference is positive, the cooling time of the white dwarf is reduced. If it is negative, the cooling time is increased. The majority of the time, $t_{\Delta} \geq 0$ and a delay is applied.

giving each white dwarf the appropriate chance of having a helium or hydrogen-dominated atmosphere.

The cooling models define the crystallised fraction of the white dwarf core. Rather than cooling continuously with time, a crystallising white dwarf will plateau in effective temperature and luminosity as energy released by crystallisation and related processes (latent heat, carbon/oxygen phase separation, and ^{22}Ne distillation) halts the cooling (Tremblay et al. 2019; Blouin et al. 2021; Saumon et al. 2022; Bauer 2023). While distillation has been found to be the main cause of the delay in the cooling process, the exact distillation delay for white dwarfs less massive than $\approx 1 M_{\odot}$ is not well understood, except that the delay seems to be peaked at a crystallised fraction of ≈ 0.5 (Kilic et al. 2020; Blouin et al. 2020; Bédard et al. 2024). In our simulation, for white dwarfs that have a crystallised fraction of ≥ 0.5 at the present day, a distillation delay of 0.5 Gyr is added to the cooling time since this process is not accounted for in the models of Bédard et al. (2020). The choice of this value is justified in Sect. 5.1. As the variation of this delay within the white dwarf population is largely unconstrained, we choose to add a small delay to all white

dwarfs as an average; we do not rule out the possibility of a larger delay applying to a smaller proportion of the white dwarf population.

Interpolation of these cooling model grids across mass, cooling time, and corresponding envelope composition gives the luminosity of each white dwarf remaining in the synthetic population. To plot the luminosity function of the synthetic population, we convert the luminosities into bolometric magnitudes, M_{bol} and bin the stars by bolometric magnitude. The simulated luminosity function using a constant star formation history in Fig. 4 shows the characteristic features of the white dwarf luminosity function: the rising slope towards fainter magnitudes, a peak at $M_{\text{bol}} \approx 15$, and then a sharp drop off due to the finite age of the population. The luminosity function is scaled to have the same number of total objects as the observed 40 pc sample.

The model-dependent observed luminosity function is calculated based on the effective temperatures and masses determined by O’Brien et al. (2024) for the 40 pc white dwarf sample with the low mass correction applied. These parameters are based on fits of *Gaia* G , G_{BP} , and G_{RP} magnitudes as well as the parallax with the appropriate model atmospheres. M_{bol} is then calculated using the cooling models of Bédard et al. (2020). The *Gaia* luminosity function has error bars that include both Poisson errors from the number of stars in each bin (\sqrt{N} where N is the number of objects in that bin) and propagated errors due to *Gaia* uncertainties on mass and effective temperature.

The reduced χ^2 (χ^2_{ν}) for the simulated luminosity function is calculated against the observed function from the 40 pc sample using:

$$\chi^2 = \sum_i^N \frac{(O_i - E_i)^2}{\sigma_i^2} \quad (4)$$

$$\chi^2_{\nu} = \frac{\chi^2}{\nu} \quad (5)$$

where the number of degrees of freedom $\nu = n - m$ is the number of observations n (here, the number of bins used in the histogram) minus the number of fitted parameters m (one, for the shape of the histogram overall), O_i is the observed frequency in the i th bin, E_i is the expected frequency in the i th bin, and σ_i is the error on the i th observation.

3.2 Absolute *Gaia* G magnitude distribution

The second method explored in this work is to compare the absolute *Gaia* G magnitude distribution to that of the synthetic population. This uses the same population synthesis method as described in the previous section until the point at which the bolometric magnitudes of the individual white dwarfs are calculated. It then diverges and uses the luminosity and effective temperature, both derived from the cooling grids of Bédard et al. (2020), combined with model atmosphere grids (Tremblay et al. 2011 for the pure hydrogen models and Cukanovaite et al. 2021 for the helium and mixed atmosphere models¹ where $\text{H/He} = 10^{-5}$) to calculate the absolute *Gaia* G magnitude for each star.

Compared to the luminosity function method, the model atmospheres are now used in the population synthesis instead of in the derivation of individual T_{eff} and mass from the observations. Most

¹ We employ the same rules as in O’Brien et al. (2023, 2024) for the use of mixed versus pure-helium model atmospheres.

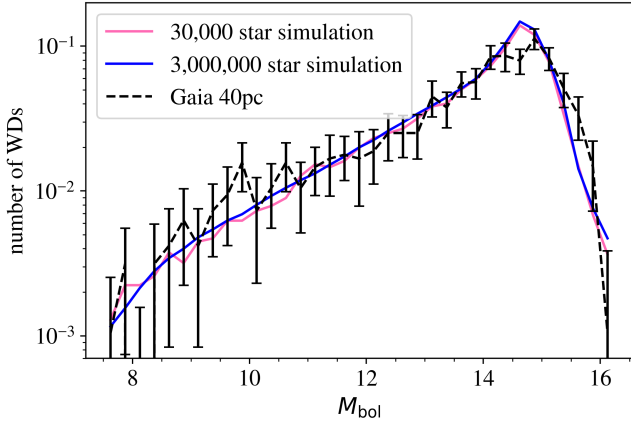


Figure 4. Observed luminosity function (black dashed line) for the 40 pc white dwarf sample compared to that of the synthetic population of white dwarfs used as the default simulation (pink solid line). A simulation including 3 000 000 stars is shown in the solid blue line. The errors on the observed 40 pc luminosity function are Poisson errors and propagation of errors from *Gaia* uncertainties on mass and effective temperature. The default synthetic luminosity function is generated with a finite number of stars therefore small oscillations in the rising slope are artifacts of the simulation process and not necessarily real features, however the 30 000 star simulation has converged (as seen by the similarity to the 3 000 000 star simulation) and so using 30 000 stars is suitable.

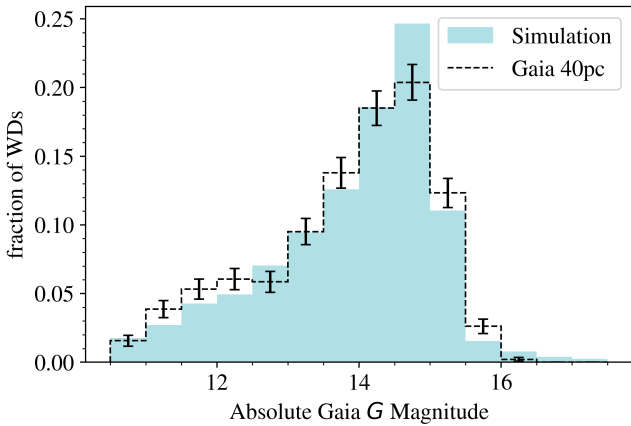


Figure 5. Observed absolute *G* magnitude distribution (black dashed line) for the 40 pc sample compared to that of the synthetic population of white dwarfs (light blue histogram). The errors on the observed 40 pc absolute *G* magnitude distribution are Poisson errors.

importantly, only observed *Gaia G* and parallax are used in the absolute *Gaia G* magnitude method, whereas *Gaia G*, G_{BP} , and G_{RP} magnitudes as well as the parallax are used in the luminosity function method, when data are fitted to obtain T_{eff} and mass.

The simulated absolute *G* magnitude distribution assuming a constant star formation history in Fig. 5 shows a peak at $M_G \approx 15$ mag, a drop off at fainter magnitudes and evidence of a bright magnitude shoulder at $M_G \approx 12.5$ mag. We calculate the χ^2_{ν} to quantify the difference with the observed distribution directly drawn from *Gaia* Data Release 3.

3.3 Direct age calculations

The direct calculation of the age of each white dwarf in the 40 pc sample requires no comparison to a simulated white dwarf population and uses the *Gaia* derived corrected effective temperatures, masses and compositions as defined by O’Brien et al. (2024). These white dwarf parameters are then converted to ages using the same models and astrophysical relations as in the previous methods. This method is based on the work of Tremblay et al. (2014), although it is adapted for the 40 pc sample.

The cooling models of Bédard et al. (2020) are employed to calculate the white dwarf cooling time. If the white dwarf has a crystallised mass fraction ≥ 0.5 , it is assumed to have experienced a distillation delay to its cooling and the white dwarf cooling age is increased by 0.5 Gyr. The pre-white dwarf mass is calculated using our modified initial-final mass relation based on the method of Cunningham et al. (2024) and then the combined main sequence and post-main sequence lifetime is calculated under an assumption of solar metallicity with BPASS models (Byrne et al. 2024). Since there is no direct evidence for individual white dwarfs in the 40 pc sample being the product of mergers or not, as the large majority of them have disc kinematics appropriate for their estimated ages (McCleery et al. 2020; Cukanovaite et al. 2023), a probabilistic approach to the merger time delay is taken. Each white dwarf is assigned a probability of being formed via merger, and those that are selected as mergers sample the cooling delay range accordingly (Temmink et al. 2020). The total age of the white dwarf is then calculated as:

$$t_{\text{total}} = t_{\text{WD}} + t_{\text{MS+GP}} + t_{\Delta} \quad (6)$$

If the inclusion of a merger delay increased the total age of the white dwarf to greater than 10.6 Gyrs, the merger delay was ignored in the calculation of the total age.

The ages of all the white dwarfs in the 40 pc sample are then binned to construct an age distribution for the population. Fig. 6 shows this histogram in a dotted blue line. The uncertainties on these bins are Poisson errors. However, this distribution is not directly the star formation history of the underlying stellar population, as it does not account for stars that will have formed in the population but that are still on the main-sequence or giant phases. It also does not account for biases due to older stars that formed in the 40 pc sample being more likely to have left the volume due to their higher space velocities on average.

To correct for the missing main sequence stars, the ratio of stars that remain main sequence stars to stars that have become white dwarfs by the present day is calculated from the Salpeter initial mass function according to Eq. 1 from Tremblay et al. (2014):

$$B_{\text{MS-WD}} = \frac{\int_{M_0}^{M_{\text{lim}}} M^{-2.35} dM}{\int_{M_{\text{lim}}}^{M_1} M^{-2.35} dM} \quad (7)$$

where M_0 and M_1 are any mass limits outside the range being studied (0.6 and $10 M_{\odot}$ respectively – as we are only interested in relative star formation history) and M_{lim} is the mass at which $t_{\text{lookback}} = t_{\text{MS+GP}}$, that is at a certain lookback time, stars of that mass have just left the asymptotic giant branch and become white dwarfs. This ratio is computed for the lookback time corresponding to the centre of each histogram bin and the number of stars in each histogram bin is adjusted to add back in these missing main sequence stars. The total number of stars is then renormalised to the total in the 40 pc sample. This corrected age distribution can be seen in Fig. 6 with the dashed blue line.

To correct for the kinematic bias meaning that older stars are

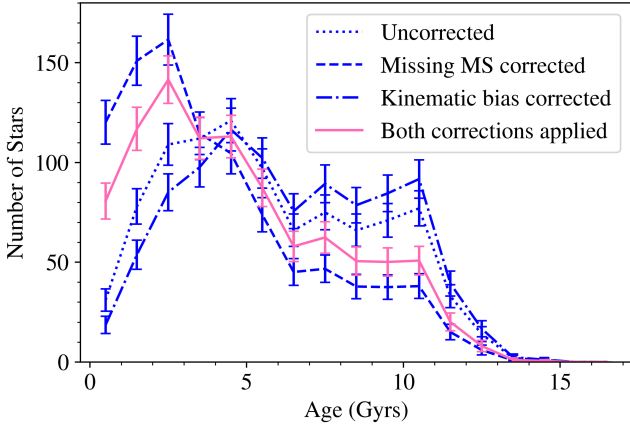


Figure 6. Number of white dwarfs in each 1 Gyr age bin with the uncorrected values in the blue dotted line and the values with both the main sequence and kinematic corrections applied in the solid pink line. Uncertainties on each bin are Poisson errors.

more likely to have left the 40 pc volume, the probability of a star remaining in the sample is calculated using Eqns. (1)-(2). For each bin, the number of stars is divided by the probability of remaining to get the original number of stars in the bin at that lookback time. As with the main sequence correction, the total number of stars is then renormalised to the total in the 40 pc sample. This kinematic-corrected distribution can be seen in the dot dashed blue line in Fig. 6.

Figure 6 shows the derived star formation history from this method with both corrections applied to the 1 Gyr width bins in a solid pink line. The resulting star formation history form finds the first stars to have formed more than 16 Gyr ago – even after having removed white dwarfs with masses less than $0.54 M_{\odot}$. These impossibly old stars could be outliers because of *Gaia* statistical uncertainties or remaining model atmosphere systematic uncertainties even after the ad-hoc mass and T_{eff} correction for $T_{\text{eff}} < 6000$ K. Due to lower mass white dwarfs having large lifetime uncertainties (Heintz et al. 2022), statistical age uncertainties on the oldest bins can be up to several Gyr. These impossibly old stars have an age within 3σ of 10.6 Gyr from *Gaia* uncertainties alone, even before we factor in systematic uncertainties from other sources, making them compatible with the 10.6 Gyr age of the Galactic disc assumed throughout. We also note that the impossibly old stars are all white dwarfs with masses very close to the $0.54 M_{\odot}$ limit. We observe a qualitative onset of stellar formation at lookback times of 10-12 Gyr, which is consistent with the age of the disc of 10.6 Gyr estimated by Cukanovaite et al. (2023) from the same sample. The star formation rate appears to increase from the onset of star formation, reaching a peak at 2–3 Gyr ago. The star formation rate appears to be about 2.5 times higher at recent times (less than 6 Gyr ago) compared to at older times.

3.4 Testing of star formation history forms

Across many data sets, methods and stellar populations, there are many derivations of the local star formation history. Two of the methods discussed in this work (the luminosity function and the absolute G magnitude distribution) rely on an underlying assumption of a star formation rate to generate a synthetic population of white dwarfs. The third method, calculating the ages of individual white dwarfs directly,

gives a star formation history by itself. To test whether all methods are consistent, we select four forms of the star formation history from previous publications to test our methods on: 1) Cukanovaite et al. (2023) which finds a constant star formation rate for the last 10.6 Gyr, 2) Mor et al. (2019) that has a star formation rate with two peaks (≈ 2.5 and 10 Gyr ago), 3) Fantin et al. (2019) that has a strong peak 9.8 Gyr ago and finally 4) we feed back our results from the direct age method (Fig. 6), which has an enhanced star formation at recent times ($\lesssim 5$ Gyr). The forms of the four star formation histories as they are approximated in this work are shown in Fig. 7.

We ran luminosity function simulations with each of the four different assumed star formation history forms and calculated the χ^2_{ν} for each with the default choices for each of the ingredients as listed in Table 1. The χ^2_{ν} values of these runs can be seen in Table 2.

The star formation history that produces a synthetic population with the best fit to the observed 40 pc sample is drawn from Mor et al. (2019), having a χ^2_{ν} 1.2 times lower than the star formation history derived in this work, the next best fit. Because these are single values of χ^2_{ν} , and at this stage we are not considering uncertainties on any ingredients in the simulation, these slight differences in χ^2_{ν} are not statistically significant. The systematic uncertainties incorporated in Sect. 4 are required before we can make statistically significant comparisons.

We also ran absolute G magnitude distribution simulations with each of the four different assumed star formation history forms and calculated the χ^2_{ν} for each in Table 2. For this method, the best fitting star formation history forms are the constant one of Cukanovaite et al. (2023), that of Mor et al. (2019), and the star formation history derived from this work which are statistically equivalent. These forms are both a significantly better fit than Fantin et al. (2019) and our direct age star formation history using this method. The issue of comparing χ^2_{ν} values as with the luminosity function method also applies here; without considering systematic uncertainties, the slight differences between the χ^2_{ν} values are not statistically significant.

These results make it clear that for a fixed set of a *Gaia*-defined stellar sample, astrophysical relations and stellar models, the derived formation history can be different depending on the methodology being used. The most likely reason for this behaviour is that the different methods rely on different subsets of *Gaia* data to reach their conclusion, which are subject to different systematics from both observations and input models. Next we evaluate what those systematics on the stellar formation history are.

4 UNCERTAINTIES

So far the synthetic populations have been generated from the fixed ingredients listed in Table 1, the default values. However in order to determine if any star formation history form is a significantly better fit to the 40 pc population than any other form, or if one of the methods under investigation is better than another, we incorporate uncertainties on these external ingredients. For each of the three methods, the code was ran with each ingredient being allowed to vary around the default values, using a Gaussian distribution unless noted otherwise, as described in the following subsections.

4.1 Systematic uncertainties

Initial mass function: By default, the simulation uses the Salpeter (1955) initial mass function with $\rho(M) \propto M^{-2.35}$ where M is the initial mass of the star and $\rho(M)$ is the initial mass density function.

Table 2. The χ^2_{ν} value found for each of the four star formation history forms when used in the Luminosity Function and Absolute G magnitude distribution methods as compared with the observed 40 pc sample. These simulations all use the default values for simulation ingredients as described in Table 1. The four star formation history forms are the approximated versions described in Sect. 3.4 and shown in Fig. 7.

Star Formation History Form	χ^2_{ν} Luminosity Function	χ^2_{ν} Absolute G Magnitude Distribution
Cukanovaite et al. 2023	3.15	2.85
Mor et al. 2019	2.47	2.99
Fantin et al. 2019	4.19	9.43
This work (Direct Age method)	3.02	4.01

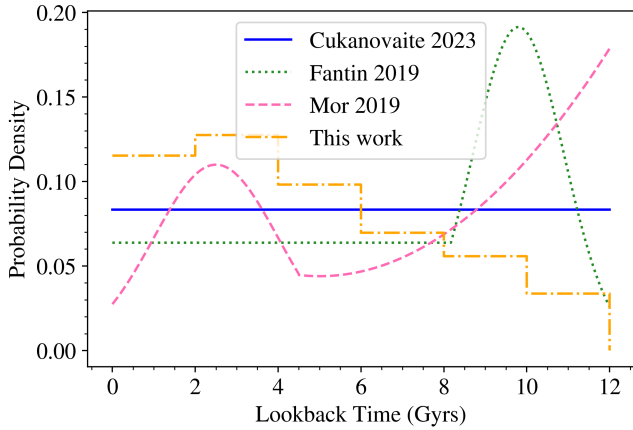


Figure 7. The four forms of star formation history used throughout this work. The four forms are approximated from Cukanovaite et al. (2023), Fantin et al. (2019), Mor et al. (2019) and the results of our direct age method. Each form has a very different shape or peaks and allows a wide range of options for our tests.

For the standard deviation, we choose a value of 0.1 (Weisz et al. 2015; El-Badry et al. 2018; Cunningham et al. 2024) on the exponent to allow the initial mass to vary around the Salpeter value but overlap with different common choices, such as Kroupa (2001) which uses $\rho(M) \propto M^{-2.3}$.

A steeper slope to the initial mass function (more negative exponent) means that the simulation will produce more low mass stars. This in turn means the simulated population will have longer main sequence lifetimes on average. A longer main sequence lifetime with the same population age and formation times means shorter white dwarf cooling times; so on average the population will have brighter magnitudes and higher effective temperatures than a population with a shallower initial mass function slope.

Main sequence lifetimes: We adopt the estimate of a 4.8 per cent uncertainty on main-sequence lifetimes from Hurley et al. (2000), independent of mass or metallicity. To incorporate this error for the systematic uncertainties, we include the same shift to all main sequence lifetimes in a given simulation run, drawing the value of the shift from a Gaussian with a standard deviation of 4.8 per cent.

By increasing the main sequence lifetime of a star and assuming the formation history remains the same, the white dwarf cooling time of the star is reduced. This means that on average, longer main sequence lifetimes result in brighter and hotter white dwarfs in the population.

Population age: In the original simulation, the age of the population is set to be 10.6 Gyr based on Cukanovaite et al. (2023), who found a

value of 10.6 ± 0.5 Gyr for the age of the local 40 pc population. Fitting the age of the 40 pc population using the Luminosity Function and the Absolute *Gaia* G Magnitude methods described here returned a wide range of ages, with the 10.6 Gyr from Cukanovaite et al. (2023) as very close to the average of our fitting results. Thus, we did not fit the population age in this work, and chose to use 10.6 Gyr as the default value in all of our simulations. For our evaluation of systematic errors, the population age is drawn from a Gaussian with a mean of 10.6 Gyr and a standard deviation of 0.7 Gyr. This standard deviation is reflective of uncertainties we found when fitting the population age as a free parameter.

By changing the age of the population (and therefore the assumed age of the Galactic disc), the age and the cooling time of the white dwarfs are also affected. An older population age allows for stars that have formed longer ago; this in turn means the white dwarfs have longer cooling ages, are cooler, and have fainter magnitudes at the present day. An older population is on average fainter with cooler effective temperatures.

Initial-final mass relation: The initial-final mass relation is derived using the method of Cunningham et al. (2024), hence from the 40 pc white dwarf sample that we also use in this work. Since the employed initial-final mass relation is already self-consistent with the *Gaia* temperature, mass and magnitude scales for the 40 pc sample, and already based on essentially the same astrophysical relations and stellar models as those used in this work, we do not vary this parameter. In other words, the initial-final relation is primarily an internal dependent relation in this work, emerging as a consequence of our particular choices of main-sequence lifetimes, initial mass function and *Gaia* photometric white dwarf masses.

We do not account for individual white dwarf mass scatter around the median initial-final mass relation, due to metallicity, magnetic field or rotation (Cunningham et al. 2024), although the scatter is expected to be at most a few per cent (Hollands et al. 2024).

Age versus velocity dispersion relation: As discussed in Sect. 3.1, older objects have a higher velocity dispersion. Because of this, they are more likely to have left a fixed volume of space close to the Galactic disc plane in the time since they formed. In the direction perpendicular to the disc plane, stars oscillate in their position with time, hence this relation can be characterised by the vertical scale height of the stars of a given age. Our default relation is based on the vertical velocity dispersion of the 40 pc white dwarfs under study as a function of age (Cukanovaite et al. 2023). However, both the ages of these white dwarfs, as well as their true velocity dispersion given the lack of radial velocities, remain uncertain. Several different age versus velocity dispersion relations have been published in the literature (Seabroke & Gilmore 2007; Buckner & Froebrich 2014; Cheng et al. 2019), including using white dwarf samples (Wegg & Phinney 2012; Raddi et al. 2022). To account for this systematic, we apply a multiplicative factor to the gradient of the scale height

relation in the age vs velocity dispersion relation, with a mean of 1.0 and a standard deviation of 0.3, sampled from a Gaussian distribution for each simulation run. This provides a wide range of assumed scale heights, reflective of the fact that this parameter is only loosely constrained. The relation always flattens off at 7 Gyrs due to the lack of kinematic information on stars of this age.

A multiplicative factor below one reduces a star’s scale height for any age, which also reduces its probability of having left the sample by the present day. This means that more old, high velocity, faint magnitude white dwarfs remain in the 40 pc simulated volume, and the population is on average fainter.

We note that white dwarfs in the local volume also show an age versus velocity dispersion relation in directions within the Galactic disc plane (Raddi et al. 2022). This suggests that our assumptions that the same number of stars come in and come out of the sample in these directions may be incorrect, and that in fact white dwarfs in the sample may have formed, on average, closer or further away to the Galactic centre (Zubiaur et al. 2024). However, this question is largely outside of the scope of this work, as we only directly constrain the stellar formation history for objects currently in the local stellar volume – and not the formation history of the Galactic disc at a specific distance to the Galactic centre – and therefore we do not need to account for this systematic. Zubiaur et al. (2024) suggest that 68 per cent of white dwarfs currently within 100 pc were formed at less than 1 kpc from the Sun, although if that interpretation was to change from a different model of radial disc migration, our results could easily be translated to this new model.

Cooling ages: The white dwarf cooling age models of Bédard et al. (2020) depend on the envelope composition and mass of the white dwarf. The cooling time in Eqn. 3 uses these models, from which the effective temperature is subsequently calculated using the same models. The cooling age for the white dwarfs in the direct calculation method is interpolated using mass, envelope composition and effective temperature from the same models.

White dwarf cooling models calculated by different groups (Camisassa et al. 2016; Camisassa et al. 2019; Bédard et al. 2020; Salaris et al. 2022; Bauer 2023; Pathak et al. 2024) cause ages to vary by several per cent due to uncertainties on core and envelope chemical compositions, atomic opacities and electronic conduction. These uncertainties do not consider the crystallisation and distillation processes which are discussed independently in the next bullet point. Therefore, we consider that the uncertainty on cooling ages is 6 per cent (Cukanovaite et al. 2023; Cunningham et al. 2024; Pathak et al. 2024). We apply a multiplicative factor to all cooling times in a given simulation run, drawing the factor from a Gaussian distribution with a mean of 1.0 and a standard deviation of 0.06. Shorter cooling ages predict a brighter and higher temperature white dwarf population on average.

Crystallisation delay: The standard white dwarf cooling models of Bédard et al. (2020) do not reproduce the full extent of the cooling delay due to crystallisation and related processes observed in the *Gaia* Hertzsprung-Russell diagram (Tremblay et al. 2019; Blouin et al. 2020; Kilic et al. 2020; Bédard et al. 2024). Our simulations use an approximation of the additional distillation delay discussed in Blouin et al. (2021) and assume that any white dwarf that has a crystallised mass fraction (as determined from the cooling models of Bédard et al. 2020) of ≥ 0.5 has experienced an additional cooling delay of 0.5 Gyr. To assess the uncertainty on this component, we employ a random binary choice between including and not including the distillation delay in a given simulation. This uncertainty is similar to the one on the cooling times detailed previously, but is only assigned to older white dwarfs that are undergoing crystallisation.

Binary evolution and stellar mergers: The simulation uses the evolutionary delays arising from the merger of binary systems from Temmink et al. (2020) as described in Sect. 3.1. As the delays already include Gaussian scatter, to assess the uncertainties here, the inclusion of mergers is randomly turned off or on for a simulation run.

In general, being a merger product lengthens either the pre-white dwarf lifetime (MS+MS mergers) or white dwarf cooling time (WD+WD mergers), and results in brighter white dwarfs at the present day. Turning off the merger delays therefore causes on average fainter white dwarfs in the population.

Spectral evolution: For the fraction of helium-atmosphere (thin hydrogen layer) white dwarfs, we adopt a standard deviation of 0.1 on the mean of 0.25 and sample from a Gaussian distribution. This accounts for both small number statistics in spectra evolution and additional uncertainties arising from subtypes with magnetic fields and metal pollution that can affect temperature and mass determinations.

The effect of changing the fraction of helium-atmosphere white dwarfs is non-linear: the interaction of composition, mass and cooling age means that He white dwarfs are not consistently brighter than H white dwarfs at the same mass and cooling age, or vice versa.

4.2 Individual star uncertainties

Metallicity: With the knowledge that the solar neighbourhood does not appear to show any age-metallicity relationship (Rebassa-Mansergas et al. 2021) except possibly for the oldest few percent of the sample (Kilic et al. 2019), we assume that the median metallicity in mass fraction of stars in the simulation is solar regardless of formation time, where $Z_{\odot} = 0.0134$ from Asplund et al. (2009). When looking at the uncertainties in this value, metallicity is sampled from a Gaussian with the mean value being solar, $Z > 0$ and the standard deviation being 0.0104 (Cunningham et al. 2024).

Gaia data errors: When simulating the white dwarf mass distribution, we alter the masses of the simulated white dwarfs by adding noise drawn from a normal distribution with a standard deviation of $0.02 M_{\odot}$ in line with the median *Gaia* statistical uncertainty on the masses from O’Brien et al. (2024). For the luminosity function and absolute *G* magnitude distribution, we instead propagate the *Gaia* error bars to the observed distributions.

4.3 Overall uncertainties

We ran a set of 100 simulations using the uncertainties described above, and 100 values of χ^2_{ν} were collected. Fig. 8 shows the spread of the 100 χ^2_{ν} values from the Luminosity Function and Absolute *G* Magnitude distribution methods from all four tested star formation histories in a box and whisker plot, as well as the results of the direct age calculations and the uncertainties on those ages when systematic and individual errors are propagated.

By comparing the χ^2_{ν} values we obtain from the default simulation ingredients (shown in Table 2) with the spread in Fig. 8, it can be seen that there are no statistically significant differences between any of the four star formation histories: the boxes representing the inter-quartile range (less than 1σ spread) overlap across the choice of star formation history, with the whiskers representing 1.5 times the inter-quartile range overlapping even further. This shows that no choice of star formation history will give a statistically better result even if the median values of χ^2_{ν} shown in pink do favour certain star formation histories over others. While it seems that the early peaking star formation history of Fantin et al. (2019) is not favoured by any

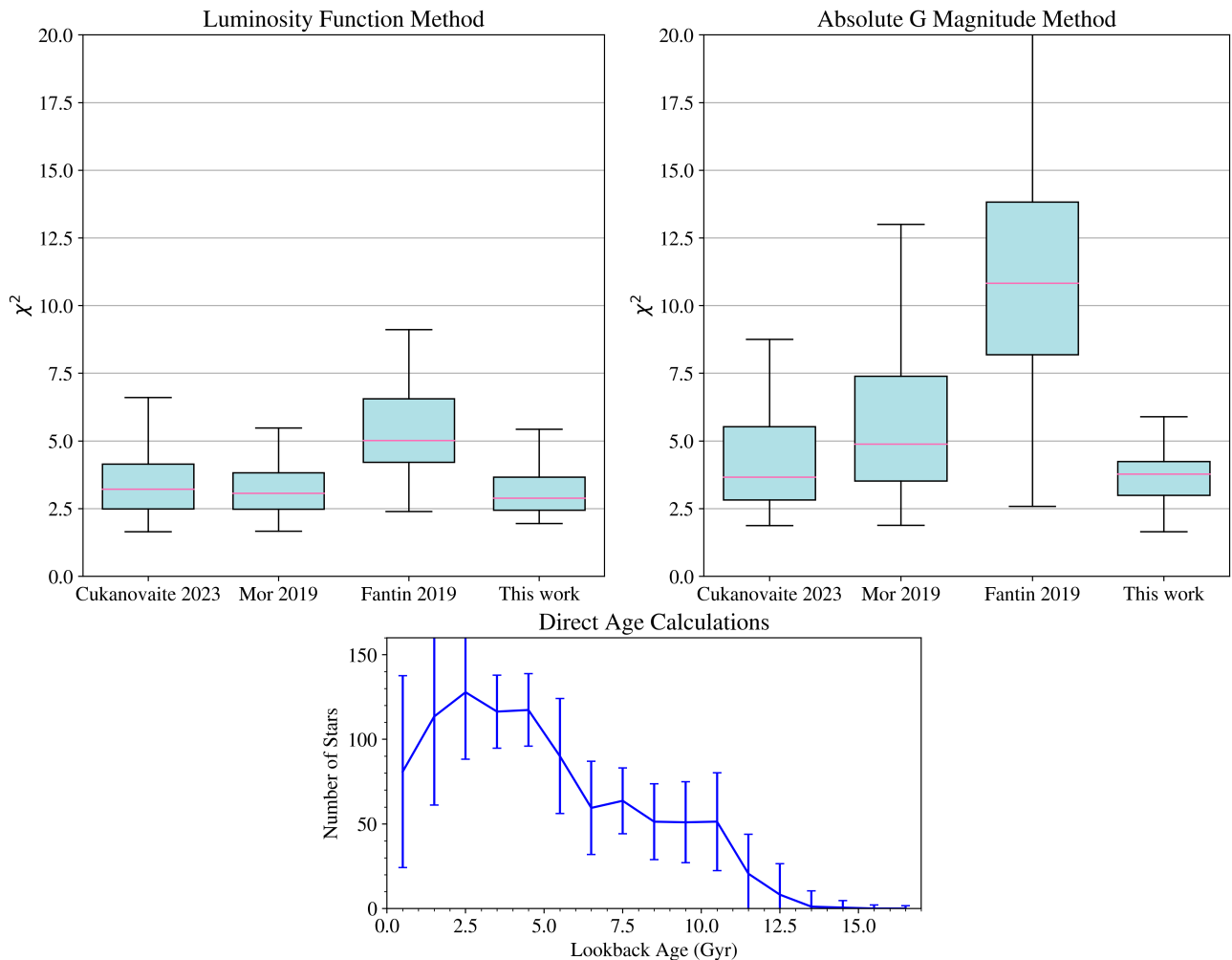


Figure 8. *Luminosity Function method:* Box and whisker plot to show the range of χ^2_{ν} values obtained from 100 runs of the Luminosity Function code including systematic uncertainties. The box extends from the first quartile to the third quartile of the data with a line at the median value (drawn in pink). The whiskers extend from the edge of the box to the furthest data point that lies within 1.5 times the inter-quartile range. Any points past the whiskers are not plotted. *Absolute G Magnitude method:* Box and whisker plots to show the range of χ^2_{ν} values obtained from 100 runs of the Absolute G Magnitude code including systematic uncertainties. The boxes and whiskers are drawn the same way as before. *Direct age calculations:* The star formation history obtained from the direct age calculation method and the systematic uncertainties on that form. Vertical errors are Poisson errors and the average spread of bin values across the 100 runs added in quadrature when systematic uncertainties and *Gaia* observational errors are applied; Poisson errors on average account for 10 per cent of the uncertainty, systematic uncertainties account for 47 per cent, and *Gaia* observational uncertainties account for 43 per cent.

of the three methods discussed here, any notable differences in the methods or star formation histories are washed out by the systematic uncertainties.

The direct age calculations also show large uncertainties due to systematics. In particular, the vertical uncertainty towards the present day makes constraining the height of the recent star formation rate enhancement difficult, and the age uncertainties with older white dwarfs can reach nearly 3 Gyr, making the onset of star formation difficult to constrain. Despite this, the enhanced star formation rate at later times appears to be significant compared to the reduced rate at earlier times.

By breaking down the uncertainties on the direct age calculations, we determine that Poisson errors account for 3–7% of the uncertainty, *Gaia* data error accounts for 43–47% of the uncertainty, and the systematics discussed in this section account for 50% of the uncertainty. Of that 50%, cooling age uncertainty is the largest contributor with 16%, followed by metallicity with 14%, and binary evolution and

stellar mergers with 10%. The other contributing sources are: age versus velocity dispersion relation, 5%; initial mass function, 3%; main sequence lifetimes, 1%; and crystallisation delay, 1%.

5 REDUCING SYSTEMATIC UNCERTAINTIES

The uncertainties on the external ingredients that are used to recover the local stellar formation history are large, multidimensional, and most likely correlated to one another. In other words, for a given *Gaia* white dwarf sample, there is a degeneracy between the luminosity function, absolute *G* magnitude distribution, functional form of the stellar formation history, and external astrophysical relations. However, it is possible to partially lift that degeneracy by comparing the observed and simulated white dwarf mass distributions. In essence, the degeneracy is partially lifted because the white

Table 3. Reduced uncertainties from comparison with the white dwarf mass distribution

Ingredient	Original uncertainty	Reduced uncertainty
Population age	$\mu = 10.6 \text{ Gyr}, \sigma = 0.7 \text{ Gyr}$	$\sigma = 0.5 \text{ Gyr}$
Initial mass function	$\mu = 2.35, \sigma = 0.1$	$\sigma = 0.075$
Initial metallicity	$\mu = 0.0134, \sigma = 0.0104$	no change
Main sequence lifetimes	multiplicative, $\mu = 1, \sigma = 0.048$	$\sigma = 0.035$
He-atmosphere WD fraction	$\mu = 0.25, \sigma = 0.1$	$\sigma = 0.065$
Merger delays	off/on, equal weighting	weighting off/on changed to 43/57
Age vs. kinematic relation	multiplicative to slope of scale height, $\mu = 1, \sigma = 0.3$	no change
Cooling models	multiplicative, $\mu = 1, \sigma = 0.06$	$\sigma = 0.045$
Crystallisation cooling delay	off/on, equal weighting	no change

dwarf mass distribution depends more on the initial mass function and main-sequence lifetimes, but much less on what happens during subsequent white dwarf evolution since white dwarf masses remain constant with time (Tremblay et al. 2016; Cunningham et al. 2024). The white dwarf mass distribution is also very well studied and so provides a robust observational sample to simulate.

To simulate the 40 pc white dwarf mass distribution, we use the same simulations as for the luminosity function and absolute G magnitude methods. However, we require fewer steps, models and assumptions, since we assume that all 40 pc white dwarfs are observed regardless of their effective temperatures (Cunningham et al. 2024), hence do not calculate a cooling age, effective temperature or distillation delay.

By calculating χ^2_{ν} values between the simulated and observed 40 pc mass distributions and only collecting the set of input parameters if $\chi^2_{\nu, \text{mass}} \leq 3$, we can examine only the simulation runs where we are guaranteed a good match to the white dwarf mass distribution. This is because $\chi^2_{\nu} = 3$ is approximately three times larger than the minimum value we find. It is worth noting that the specific choice of 3 does not affect the outcomes here: limiting χ^2_{ν} to any value 2–6 achieves a very similar limit on the uncertainty parameter space. We then take a closer look at the values for the ingredients that passed such quality criteria.

For a constant star formation history, we collected 100 simulation runs that also meet our $\chi^2_{\nu, \text{mass}} \leq 3$ criteria. Table 3 compares the input sampled uncertainties with the spread of output values for each ingredient, i.e. our *reduced* uncertainties.

The results shown indicate that the original uncertainties on population age, initial mass function, main sequence lifetimes, helium-and atmosphere fraction, the inclusion of merger delays, and cooling ages were overestimated compared to what is allowed by the 40 pc white dwarf mass distribution. The ingredients that experienced no change are typically those that do not affect the shape of the white dwarf mass distribution. We also note that the initial-final mass relation is fixed in our study and based on most of the same ingredients as those used in this work. While this biases the results towards the selected median slope of the initial mass function, model main-sequence lifetimes and population age, we make no claim of constraining the absolute value of these three quantities in this work, and instead the self-consistent initial-final mass relation allows us to constrain the size of the error bars on all ingredients.

We ran the code for the luminosity function and absolute G magnitude methods and different formation histories again as in Fig. 8 with the reduced uncertainties as determined by restricting the $\chi^2_{\nu, \text{mass}}$.

Fig. 9 shows that this does reduce the spread and location of the box and whisker plot as expected.

5.1 Sub-samples of massive white dwarfs

Another way to test systematic uncertainties is to look at the stellar formation history for white dwarfs above a certain mass threshold, with the higher mass white dwarfs having smaller main sequence lifetimes, and smaller uncertainties on their main sequence lifetimes owing to the steep inverse correlation of this parameter with mass. In the past, studies have used a cut-off at either $0.63 M_{\odot}$ (Heintz et al. 2022) or $0.9 M_{\odot}$ (Isern 2019). We note, however, that recent studies have also shown that higher mass white dwarfs may have higher uncertainties on their cooling ages from a higher fraction of stellar mergers (Temminck et al. 2020; Bédard et al. 2024; Jewett et al. 2024).

Cheng et al. (2019) showed that 5–9 per cent of ultra-massive white dwarfs ($1.08\text{--}1.23 M_{\odot}$) experience a cooling delay of at least 8 Gyr, which produces the high mass portion of the Q branch in the Hertzsprung-Russell diagram. Bédard et al. (2024) demonstrated that this long delay is the result of distillation in white dwarfs with high core ^{22}Ne abundances, arising from either high-metallicity progenitors or stellar mergers. However, distillation may also occur in white dwarfs descending from solar-metallicity progenitors and thus having a standard ^{22}Ne content, leading to much shorter delays (Blouin et al. 2021; Venner et al. 2023). Our simulations consider the latter scenario by assuming that all crystallising white dwarfs experience an additional 0.5 Gyr distillation delay to their cooling. However, the small population of extra-delayed massive white dwarfs cannot be probed using the 40 pc sample, as the $>0.9 M_{\odot}$ sub-sample only contains 66 white dwarfs. Hence, small number statistics prevents us from testing different delay scenarios and resulting formation histories for that mass range.

We can still test the impact of different distillation delays on the full 40 pc population. We find that extrapolating the scenario of Bédard et al. (2024) to all white dwarf masses (that is, 7 per cent of all white dwarfs experience a cooling delay of 8 Gyr) makes no significant differences to the predicted luminosity function and absolute G magnitude distribution. This is largely a consequence of crystallising white dwarfs of all masses having a wide range of absolute magnitudes. The most pronounced effect of the distillation delay is seen instead in the predicted two-dimensional mass versus T_{eff} distribution (Kilic et al. 2025). However, we also find in that case that the two choices of distillation delays discussed in this section – 0.5 Gyr for all

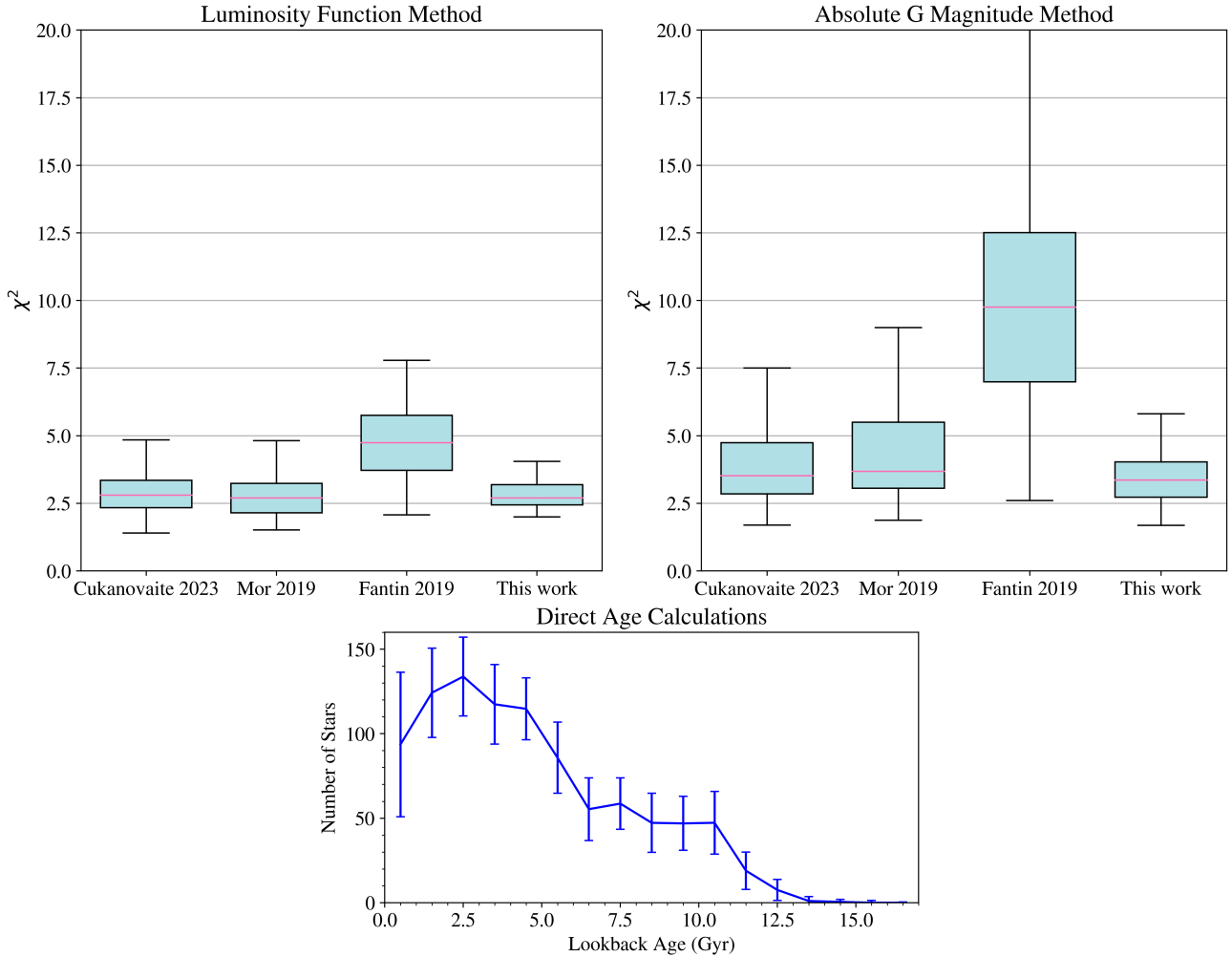


Figure 9. Same as Fig. 8, but with the reduced systematic uncertainties given in Table 3 after the additional step of comparing the population synthesis with the observed 40 pc mass distribution.

or 8 Gyr for 7 per cent of white dwarfs – are largely degenerate. The main difference between the two delay types concerns the inferred population age, as a systematic 0.5 Gyr delay results in fewer faint simulated white dwarfs compared to the case of a longer delay for a fraction of white dwarfs. However, the uncertainties on the inferred age of the population are of the same order as the distillation delay, making any conclusion difficult.

Another way to test distillation delay effects is using kinematics. However, the large majority of white dwarfs in the 40 pc sample have disc kinematics appropriate for their estimated ages (McCleery et al. 2020; Kilic et al. 2020; Cukanovaite et al. 2023). Since the average total age is large, at ≈ 5 Gyr, a moderate cooling delay of several Gyrs will only increase the total age by a modest factor, hence such delay is not expected to have a strong signature on the kinematics of the full 40 pc sample. As a consequence, observed kinematics offer weak constraints on the distillation delay of average mass white dwarfs (Kilic et al. 2020). This is different to the massive sub-sample where the distilling white dwarfs have short main-sequence lifetimes and cooling ages, hence a proportionally much larger distillation delay.

To minimise uncertainties from stars having long and uncertain main-sequence lifetimes, we investigated the effect of applying a cut-off of $>0.63 M_{\odot}$ in white dwarf masses in both the population synthesis and observed sample, at the expense of having $\approx 40\%$ larger

Poisson errors. This experiment reveals that the constant star formation history form remains the best fitting star formation history on the smaller sub-samples, the same as for the full 40 pc sample. This smaller sample does produce higher χ^2_{ν} than the full 40 pc sample, and the systematic uncertainties remain large, making it difficult to assess whether one star formation history is significantly better than the others in much the same way as with the full simulations. We conclude that high mass sub-samples are not key to extracting a more precise stellar formation history.

6 CONCLUSIONS

We have investigated three methods of determining the star formation history from a white dwarf population: the luminosity function, absolute G magnitude distribution and direct age calculations. We find that the systematic uncertainties on main-sequence, post-main-sequence and white dwarf models, as well as astrophysical relations such as the initial mass function and age versus velocity dispersion relation, dominate over any underlying differences between the methods. All three methods and their best fit star formation histories agree with one another within errors. This suggests that the choice of which

method to use should be influenced by which data are available to use. For instance, the absolute G magnitude method only requires a magnitude and a parallax for each white dwarf, and does not require individual white dwarf temperatures or masses. The method may therefore be better suited for larger white dwarf samples that do not have extensive follow-up spectroscopy. As the systematic uncertainties on any of the three methods are large, the focus of future work should be on reducing uncertainties on input stellar and Galactic models where possible to better constrain simulations of white dwarf populations. In particular, we suggest a focus on reducing the uncertainties on white dwarf cooling times, merger delays, the local stellar metallicity distribution, and the scale height of the Galactic disc as a function of age.

We explored four forms of star formation histories of the Galactic disc for the last 10.6 Gyr throughout this paper; a first one derived from our direct age calculations, Fantin et al. (2019); Mor et al. (2019); Cukanovaite et al. (2023). These are 1) peaking at recent times, 2) peaking at old times, 3) double peaked or 4) constant, respectively, with the maximum and minimum formation rates at any time different at most by a factor of three.

We note that the star formation history of Fantin et al. (2019) which peaks at old times does give a worse fit with the 40 pc sample using both the Absolute G Magnitude and Luminosity Function methods, and disagrees with the Direct Age method which finds a star formation history that peaks at recent times. This worse fit is not statistically significant, however, due to the size of the systematic uncertainties.

The star formation history derived in this work via the Direct Age method agrees with the constant star formation history of Cukanovaite et al. (2023) within 2σ , and both star formation histories have similar χ^2_ν fits with the 40 pc sample, making it difficult to quantitatively say which is favoured by the 40 pc sample.

Due to this lack of a statistically significant best fit across the three fitting methods and four forms of stellar formation histories explored, we agree with the conclusion of Cukanovaite et al. (2023) that a constant star formation rate is advised as the most simple, default scenario for simulations of the 40 pc sample and more broadly for the star formation rate of the local Milky Way. We also present tentative evidence that star formation histories with early peaks should be avoided. These results will hopefully guide future simulations and interpretations of volume-limited stellar samples in the Solar neighbourhood.

ACKNOWLEDGEMENTS

This research received funding from the European Research Council under the European Union’s Horizon 2020 research and innovation programme number 101002408 (MOS100PC). AB is a Postdoctoral Fellow of the Natural Sciences and Engineering Research Council (NSERC) of Canada. TC was supported by NASA through the NASA Hubble Fellowship grant HST-HF2-51527.001-A awarded by the Space Telescope Science Institute, which is operated by the Association of Universities for Research in Astronomy, Inc., for NASA, under contract NAS5-26555. This work has made use of data from the European Space Agency (ESA) mission Gaia (<https://www.cosmos.esa.int/gaia>), processed by the Gaia Data Processing and Analysis Consortium (DPAC, <https://www.cosmos.esa.int/web/gaia/dpac/consortium>). Funding for the DPAC has been provided by national institutions, in particular the institutions participating in the Gaia Multilateral Agreement.

DATA AVAILABILITY STATEMENT

The observational data used in this article are published in McCleery et al. (2020); Gentile Fusillo et al. (2021) and O’Brien et al. (2024). The results derived in this article will be shared on a reasonable request to the corresponding author.

REFERENCES

- Alzate J. A., Bruzual G., Díaz-González D. J., 2021, *MNRAS*, **501**, 302
 Antoja T., et al., 2018, *Nature*, **561**, 360
 Asplund M., Grevesse N., Sauval A. J., Scott P., 2009, *Annual Review of Astronomy and Astrophysics*, **47**, 481–522
 Bauer E. B., 2023, *ApJ*, **950**, 115
 Bédard A., 2024, *Ap&SS*, **369**, 43
 Bédard A., Bergeron P., Brassard P., Fontaine G., 2020, *ApJ*, **901**, 93
 Bédard A., Brassard P., Bergeron P., Blouin S., 2022, *ApJ*, **927**, 128
 Bédard A., Blouin S., Cheng S., 2024, *Nature*, **627**, 286
 Bergeron P., Dufour P., Fontaine G., Coutu S., Blouin S., Genest-Beaulieu C., Bédard A., Rolland B., 2019, *ApJ*, **876**, 67
 Blouin S., Daligault J., Saumon D., Bédard A., Brassard P., 2020, *A&A*, **640**, L11
 Blouin S., Daligault J., Saumon D., 2021, *ApJ*, **911**, L5
 Blouin S., Bédard A., Tremblay P.-E., 2023, *MNRAS*, **523**, 3363
 Buckner A. S. M., Froebrich D., 2014, *MNRAS*, **444**, 290
 Byrne C. M., Eldridge J. J., Stanway E. R., 2024, BPASS stellar evolution models incorporating α -enhanced composition – I. Single star models from 0.1 to 316 M_\odot ([arXiv:2410.23167](https://arxiv.org/abs/2410.23167)), <https://arxiv.org/abs/2410.23167>
 Camisassa M. E., Althaus L. G., Córscico A. H., Vinyoles N., Serenelli A. M., Isern J., Bertolami M. M. M., García-Berro E., 2016, *ApJ*, **823**, 158
 Camisassa M. E., et al., 2019, *A&A*, **625**, A87
 Camisassa M., Torres S., Hollands M., Koester D., Raddi R., Althaus L. G., Rebassa-Mansergas A., 2023, *A&A*, **674**, A213
 Caron A., Bergeron P., Blouin S., Leggett S. K., 2023, *MNRAS*, **519**, 4529
 Cheng S., Cummings J. D., Ménard B., 2019, *ApJ*, **886**, 100
 Cignoni M., Degl’Innocenti S., Prada Moroni P. G., Shore S. N., 2006, *A&A*, **459**, 783
 Cukanovaite E., Tremblay P.-E., Bergeron P., Freytag B., Ludwig H.-G., Steffen M., 2021, *MNRAS*, **501**, 5274
 Cukanovaite E., Tremblay P. E., Toonen S., Temmink K. D., Manser C. J., O’Brien M. W., McCleery J., 2023, *MNRAS*, **522**, 1643
 Cummings J. D., Kalirai J. S., Tremblay P.-E., Ramirez-Ruiz E., Choi J., 2018, *ApJ*, **866**, 21
 Cunningham T., Tremblay P.-E., Gentile Fusillo N. P., Hollands M., Cukanovaite E., 2020, *MNRAS*, **492**, 3540
 Cunningham T., Tremblay P.-E., W. O’Brien M., 2024, Initial-final mass relation from white dwarfs within 40 pc ([arXiv:2310.15410](https://arxiv.org/abs/2310.15410)), [doi:10.1093/mnras/stad3275](https://doi.org/10.1093/mnras/stad3275)
 Dal Tio P., et al., 2021, *MNRAS*, **506**, 5681
 Di Matteo P., Bournaud F., Martig M., Combes F., Melchior A. L., Semelin B., 2008, *A&A*, **492**, 31
 El-Badry K., Rix H.-W., Weisz D. R., 2018, *ApJ*, **860**, L17
 Eldridge J. J., Stanway E. R., Xiao L., McClelland L. A. S., Taylor G., Ng M., Greis S. M. L., Bray J. C., 2017, *Publ. Astron. Soc. Australia*, **34**, e058
 Fantin N. J., et al., 2019, *ApJ*, **887**, 148
 Gaia Collaboration et al., 2016a, *A&A*, **595**, A1
 Gaia Collaboration et al., 2016b, *A&A*, **595**, A2
 Gaia Collaboration et al., 2018, *A&A*, **616**, A1
 Gaia Collaboration et al., 2021, *A&A*, **649**, A1
 Gallart C., et al., 2024, *A&A*, **687**, A168
 Gentile Fusillo N. P., et al., 2019, *MNRAS*, **482**, 4570
 Gentile Fusillo N. P., et al., 2021, *MNRAS*, **508**, 3877
 Haywood M., Lehnert M. D., Di Matteo P., Snaith O., Schultheis M., Katz D., Gómez A., 2016, *A&A*, **589**, A66
 Haywood M., Di Matteo P., Lehnert M., Snaith O., Fragkoudi F., Khoperskov S., 2018, *A&A*, **618**, A78

Heintz T. M., Hermes J. J., El-Badry K., Walsh C., van Saders J. L., Fields C. E., Koester D., 2022, *ApJ*, **934**, 148

Helmi A., Babusiaux C., Koppelman H. H., Massari D., Veljanoski J., Brown A. G. A., 2018, *Nature*, **563**, 85

Hollands M. A., Littlefair S. P., Parsons S. G., 2024, *MNRAS*, **527**, 9061

Hurley J. R., Pols O. R., Tout C. A., 2000, *MNRAS*, **315**, 543

Iben Icko J., Ritossa C., García-Berro E., 1997, *ApJ*, **489**, 772

Isern J., 2019, *ApJ*, **878**, L11

Jewett G., et al., 2024, *ApJ*, **974**, 12

Jiménez-Esteban F. M., Torres S., Rebassa-Mansergas A., Skorobogatov G., Solano E., Cantero C., Rodrigo C., 2018, *MNRAS*, **480**, 4505

Kalirai J. S., 2012, *Nature*, 486, 90–92

Khoperskov S., Haywood M., Di Matteo P., Lehnert M. D., Combes F., 2018, *A&A*, **609**, A60

Kilic M., Bergeron P., Dame K., Hambly N. C., Rowell N., Crawford C. L., 2019, *MNRAS*, **482**, 965

Kilic M., Bergeron P., Kosakowski A., Brown W. R., Agüeros M. A., Blouin S., 2020, *ApJ*, **898**, 84

Kilic M., Bergeron P., Blouin S., Moss A., Brown W. R., Bédard A., Jewett G., Agüeros M. A., 2025, *ApJ*, **979**, 157

Kroupa P., 2001, *MNRAS*, **322**, 231

Ludwig H.-G., Caffau E., Steffen M., Bonifacio P., Sbordone L., 2010, *A&A*, **509**, A84

Marigo P., et al., 2020, *Nature Astronomy*, **4**, 1102–1110

McCleery J., et al., 2020, *MNRAS*, **499**, 1890

Mestel L., 1952, *MNRAS*, **112**, 583

Mor R., Robin A. C., Figueras F., Roca-Fàbrega S., Luri X., 2019, *A&A*, **624**, L1

O’Brien M. W., et al., 2023, *MNRAS*, **518**, 3055

O’Brien M. W., et al., 2024, *MNRAS*, **527**, 8687

Pathak P., Blouin S., Herwig F., 2024, *arXiv e-prints*, p. arXiv:2410.14014

Raddi R., et al., 2022, *A&A*, **658**, A22

Rebassa-Mansergas A., et al., 2021, *MNRAS*, **505**, 3165

Rieke G. H., Alonso-Herrero A., Weiner B. J., Pérez-González P. G., Blaylock M., Donley J. L., Marcillac D., 2009, *ApJ*, **692**, 556

Rolland B., Bergeron P., Fontaine G., 2018, *ApJ*, **857**, 56

Rowell N., 2013, *MNRAS*, **434**, 1549

Rowell N., Kilic M., 2019, *MNRAS*, **484**, 3544

Salaris M., Cassisi S., Pietrinferni A., Hidalgo S., 2022, *MNRAS*, **509**, 5197

Salim S., et al., 2007, *ApJS*, **173**, 267

Salpeter E. E., 1955, *ApJ*, **121**, 161

Saumon D., Blouin S., Tremblay P.-E., 2022, *Physics Reports*, **988**, 1

Schröder K. P., Pauli E. M., Napiwotzki R., 2004, *MNRAS*, **354**, 727

Seabroke G. M., Gilmore G., 2007, *MNRAS*, **380**, 1348

Soderblom D. R., 2010, *ARA&A*, **48**, 581

Stanway E. R., Eldridge J. J., 2018, *MNRAS*, **479**, 75

Stewart K. R., Bullock J. S., Wechsler R. H., Maller A. H., Zentner A. R., 2008, *ApJ*, **683**, 597

Temink K. D., Toonen S., Zapartas E., Justham S., Gänsicke B. T., 2020, *A&A*, **636**, A31

Toonen S., Hollands M., Gänsicke B. T., Boekholt T., 2017, *A&A*, **602**, A16

Tremblay P. E., Bergeron P., Gianninas A., 2011, *ApJ*, **730**, 128

Tremblay P.-E., Kalirai J. S., Soderblom D. R., Cignoni M., Cummings J., 2014, *ApJ*, **791**, 92

Tremblay P.-E., Cummings J., Kalirai J. S., Gänsicke B. T., Gentile-Fusillo N., Raddi R., 2016, *MNRAS*, **461**, 2100

Tremblay P.-E., et al., 2019, *Nature*, **565**, 202–205

Venner A., Blouin S., Bédard A., Vanderburg A., 2023, *MNRAS*, **523**, 4624

Vincent O., Barstow M. A., Jordan S., Mander C., Bergeron P., Dufour P., 2024, *A&A*, **682**, A5

Wegg C., Phinney E. S., 2012, *MNRAS*, **426**, 427

Weisz D. R., Skillman E. D., Cannon J. M., Dolphin A. E., Kennicutt Robert C. J., Lee J., Walter F., 2008, *ApJ*, **689**, 160

Weisz D. R., et al., 2015, *ApJ*, **806**, 198

Winget D. E., Hansen C. J., Liebert J., van Horn H. M., Fontaine G., Nather R. E., Kepler S. O., Lamb D. Q., 1987, *ApJ*, **315**, L77

Zubiaur A., Raddi R., Torres S., 2024, *A&A*, **687**, A286

This paper has been typeset from a $\text{\TeX}/\text{\LaTeX}$ file prepared by the author.